Vacancy-Induced Resistive Switching and Synaptic Behavior in flexible BST@C_f memristor crossbars

Ze Wang[a,b], Jianling Yue[a,b], Chao Jiang[a,b,*], Isaac Abrahams[c], Yantao Yu[a,b], Yunxin Li[d], Zuojuan Du[a,b], Xiaozhong Huang[a,b], Linling Li[e], Guangyuan Wang[e], Hao Zhou[e]

[a] Institute of Aeronautics and Astronautics, Central South University, Changsha 410012, China

[b] Key Lab for Advanced Fibers and Composites of Hnnan Province, Changsha 410012, China

[c] School of Biological and Chemical Sciences, Queen Mary University of London, London E1 4NS, UK

[d] School of Materials Science and Engineering, Northeastern, Northeastern University, Shenyang 110819, China

[e]Beijing Institute of Spacecraft System Engineering, China Academy of Space Technology, Beijing 100094, China

*Corresponding author: jiangchao@csu.edu.cn (Chao Jiang)

Abstract: In this study, carbon fibers (C_f) coated with $Ba_{0.6}Sr_{0.4}TiO_3$ (BST) (BST@C_f) were prepared by magnetron sputtering and subsequently heated in nitrogen to produce oxygen vacancies. BST@C_f and nitrogen-treated BST@C_f were cross-stacked on polyimide (PI) film to make a BST@C_f memristor. The electrical

properties of BST@C_f memristor were measured after being bent 3000 times. The device exhibits bipolar figure-of-eight (f8) hysteresis loop characteristics under applied voltage. The hysteresis loops narrow with increasing temperature of heat treatment in nitrogen, due to decrease in oxygen vacancy concentration. The hysteresis loops demonstrate the switching process of resistance between high resistance state (HRS) and low resistance state (LRS), with a maximum HRS/LRS ratio of 10^6. The switching process can be divided into two parts, corresponding to Schottky Emission and Fowler-Nordheim (F-N) Tunneling. It is notable that no electroforming voltage is required to stimulate the memristor. The constructed memristor was cycled successfully 1000 times and retained the LRS 787 s during power cut off. In addition, the device exhibited synaptic behavior including learning and forgetting processes, in accordance with the paired-pulse facilitation (PPF) rule. The use of BST@C_f in the construction of the nonvolatile memristor imparts flexibility to the device allowing for the possibility of wearable flexible intelligent memristor based electronic devices in the future.

Keywords: Flexible memristor, Barium strontium titanate, Carbon fiber, No electroforming voltage, Synaptic behavior

1. Introduction

The development of semiconductor technology has followed Moore's law, where the density of components in an integrated circuit double every 18-24 months. However, silicon-based materials are approaching their physical limits [1-3]. Memristors are considered to be promising candidates for replacing existing silicon based electronic components allowing for alternatives to von Neumann architecture. This is attributed to their excellent characteristics such as being highly scalable, with low power consumption, a fast response rate, excellent cyclability and possessing a non-volatile memory [4-14]. Moreover, memristors have very similar characteristics to the learning and memory processes of the human synapse. The resistance of memristors varies with the magnitude and duration of the applied voltage, which can mimic human synaptic plasticity in a single unit [15-18], while traditional electronic circuits require many electronic components and software programs to simulate a synapse.

Flexible memristors have attracted considerable attention due to the possibility of constructing wearable devices. Ultra-flexible egg albumen was used by Zhou et al. [10] to fabricate a wearable protein based memristor array, which exhibited excellent memory behavior. Vu et al. [19] used MoS_2 and graphene prepared by chemical vapor deposition (CVD) and photolithography technologies to produce a flexible memristor array with a high-on/off-ratio floating-gate. Burgt et al. [20] utilized polyetherimide (PEI) and poly(3,4-ethylenedioxythiophene) (PEDOT) to fabricate a fully-organic

memristor as a low-voltage artificial synapse. Indeed, most flexible memristors reported are based on organic films prepared using conventional lithography technology, which lifts off plenty of the materials during the manufacturing process for fabricating memristor crossbars [21], while fiber based flexible memristors can retain almost all coating materials.

Fiber based electronic devices are viewed as promising candidates for flexible electronic textiles (e-textiles), due to their soft, wearable, breathable and washable characteristics [22,23]. Carbon fiber is an outstanding electronic material due to its high stiffness, high tensile strength, low weight, high chemical resistance, high conductivity and excellent heat dissipation performance [24-26]. Zhou et al. [14] demonstrated carbon fiber to be an outstanding material for fabricating memristors. However, to date, few studies have focused on carbon fiber based flexible memristors [26]. Our group previously reported a flexible $TiO_2@C_f$ memristor based on carbon fiber, prepared via a hydrothermal method [27], which shows excellent memristor characteristics. While that work provided a simple path to fabricate flexible wearable memristors, the mechanical properties of carbon fibers are reduced due to the treatment at high temperature and pressure during the hydrothermal reaction.

Barium strontium titanate (BST) is an excellent electronic material usually used as a tunable phase shifter, antenna and dynamic random access memory (DRAM) material due to its moderate relative dielectric permittivity, high tunability, low dielectric loss and high-quality factor [28-32]. Hwang et al. [33] reported an

ultra-large-scale integrated DRAM based on BST, which showed low dielectric loss and leakage current. The DRAM is based on the capacitive storage properties of BST, which must be frequently refreshed to prevent information loss. However, Li et al. [34] found that refreshing is not required in memristors based on BST coated silicon wafer. To date, there have been no reports of BST based flexible memristors.

In this work, carbon fibers (C_f) magnetron sputtered with $Ba_{0.6}Sr_{0.4}TiO_3$ (BST) were cross-stacked with nitrogen-treated BST@C_f on polyimide (PI) film to make a BST@C_f memristor. The device exhibits both digital switching and synaptic behavior, with the switching ratio between low resistance and high resistance states (HRS/LRS) reaching a maximum of 10^6 and significantly no electroforming voltage required to stimulate the memristor.

2. Experimental section

The raw carbon fibers were calcined at 500 °C for 1 h under nitrogen and then washed ultrasonically in ethyl alcohol and deionized water for 10 min to remove the polymer covering and trace impurities on the surfaces of the fibers. $Ba_{0.6}Sr_{0.4}TiO_3$ was deposited on two sides of carbon fibers by radio frequency magnetron sputtering with BST target materials (Y.X Chen 99.9%) in argon atmosphere. The working pressure, power and time per fiber side were 0.5 MPa, 800 W and 40 min, respectively. A patterned mask was attached to a PI (polyimide) film (J. Kai, thickness 0.06 mm) and Cu electrodes deposited on the film by DC magnetron sputtering at 800 W at a

working pressure of 0.5 MPa for 5 min. Some of the coated fibers were calcined for 3h at 473, 573, 673 or 773 K under flowing nitrogen to produce samples of different oxygen vacancy concentration. Fibers of untreated BST@C_f were placed across nitrogen-treated BST@C_f on PI film which was previously plated with copper electrodes (ca. 2.5 mm × 6 mm). The end of each fiber was fixed to the copper electrode by conductive silver paste. Four sets of memristors were produced using the different nitrogen-treated BST@C_f and are denoted as H_1, H_2, H_3 and H_4, corresponding to nitrogen treatments at or 473, 573, 673 or 773K, respectively. The constructed memristor is shown schematically in Fig. 1.

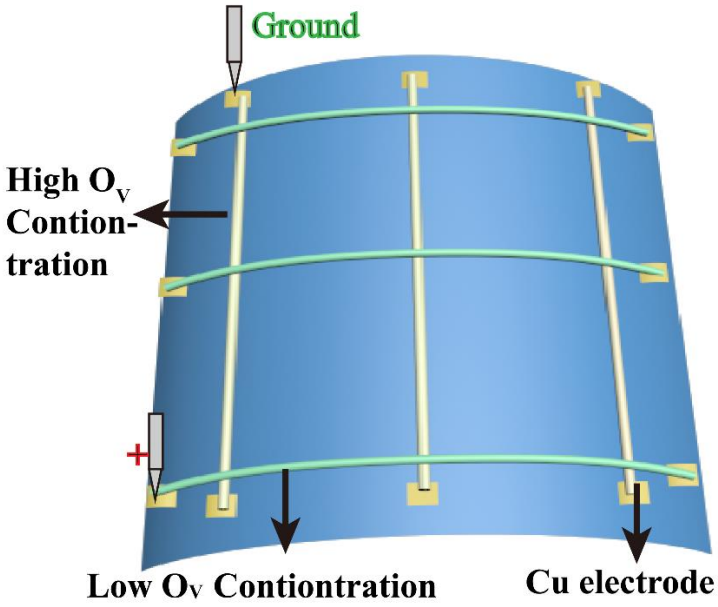

Fig. 1. Schematic diagram of BST@C_f memristor.

Fiber thicknesses were measured by transmission electron microscope (TEM, FEI Tecnai G2 F20), while the surface morphology was observed by scanning electron microscopy (SEM, TESCAN MIRA3 LMU). Surface element and oxygen vacancy concentrations were detected by X-ray photoelectron spectroscopy (ThermoFischer

EscaLab Xi+). Electrical characterization was carried out using a Keithley 4200-SCS parameter analyzer. Synapse mimicking was tested using an Agilent B1500A semiconductor device analyzer.

3. Results and discussion

3.1 Characterization techniques

Fig. 2(a) shows an SEM image of BST@C_f fibers, with a cross-section of a single fiber shown in Fig. 2(b) and crossed fibers in a constructed memristor shown in Fig. 2(c). The diameter of the carbon fibers is about 7 μm, with a smooth surface of the BST coating. The BST coating is too thin to be accurately measured by SEM and therefore for this TEM was employed, revealing a thickness of ca. 38 nm (Fig. 2(d)).

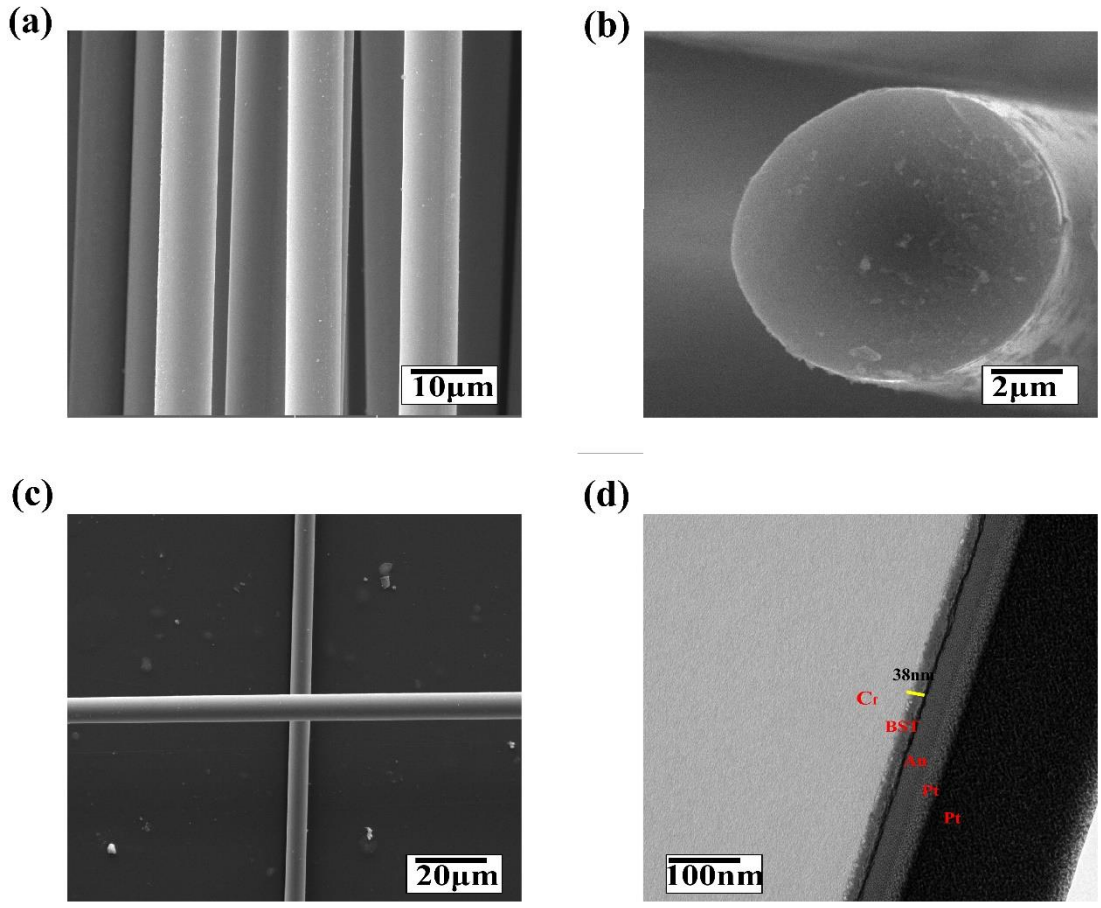

Fig. 2. SEM image of (a) surface of BST@C_f, (b) transverse section of BST@C_f and (c) the

top-view of contact point of two cross assembled fibers with different oxygen vacancy concentration. (d) TEM image of BST@C_f after FIB thinning, the Au and Pt coatings are deposited during FIB thinning.

Argon ion etching X-ray photoelectron survey (XPS) technology is used to test the element information of the BST coating. XPS spectra for Ba 3*d*, Sr 3*d* and Ti 2*p* are shown in Figs. 3(a) to 3(c), respectively. XPS spectra for O 1*s* of un-annealed BST@C_f is shown in Fig. 3(d). The Ba 3d spectra were fitted into two pairs of $3d_{5/2}$ $3d_{3/2}$ doublets with a splitting of 15.3 eV and an area ratio of 2/3 between the spin-orbit pairs. The lower binding species is attributed to Ba in BST, while the higher binding energy species is attributed to BaO or $BaCO_3$. The results are in good agreement with previous studies on BST [35]. The binding energies show an initial decrease from 473 K to 773 but then a steady increase thereafter. Similarly, the fraction of the total Ba present as BST (estimated from the integrated peak areas) reaches a minimum in the sample at 473 K and then shows a steady increase up to 773 K, but is never more than ca. 50%. A similar trend of binding energies is seen in the Sr 3*d* and Ti 2*p* spectra. Interestingly while the Ti 2*p* spectra show only a single species at all temperatures, the Sr 3*d* spectra only show this up to 673 K, while at 773 K the data can be modeled on at least 3 species. The exact identity of these species is unknown, however the spectrum at 773 K is not unlike that presented by Rodrigues et al [36] after annealing BST at 1073 K, where up to four different Sr species were identified.

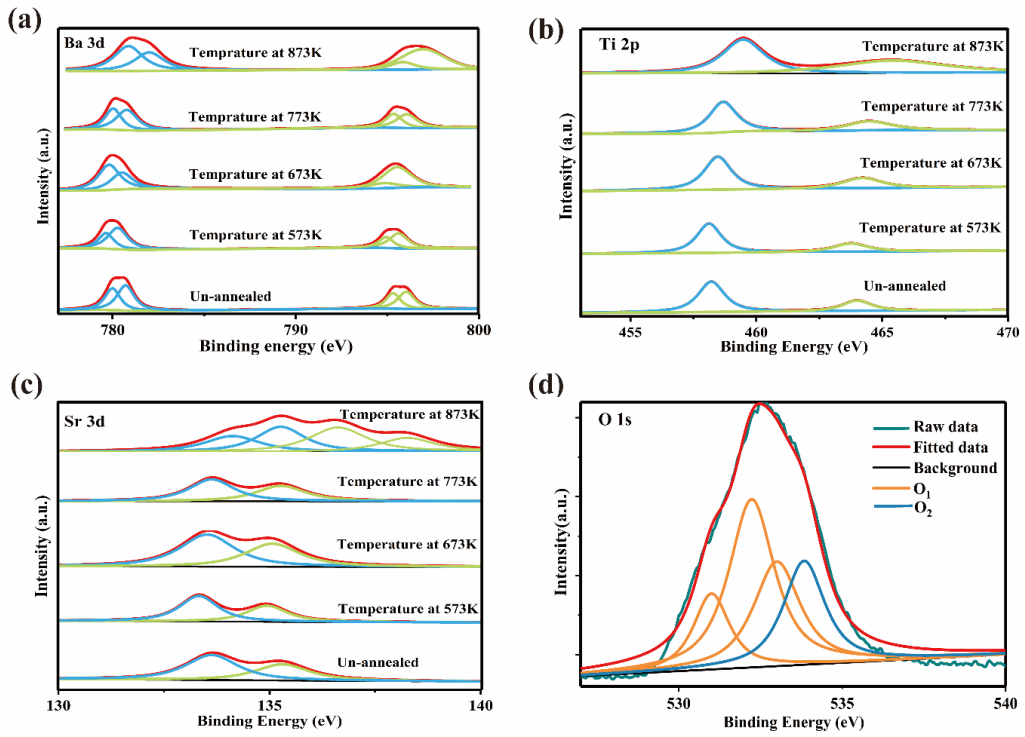

Fig. 3. (a) XPS spectra of the surface BST@C_f heated at four different temperatures for (a) Ba 3*d*, (b) Sr 3*d*, (c) and Ti 2. (d) XPS spectra of surface of un-annealed BST@C_f for O 1*s*.

Fig. 4(a) to Fig. 4(d) show the fitted O 1*s* spectra for BST@C_f samples annealed at the four studied temperatures. According to the research of Fujisaki et al. [35], the surface of BST film is mainly $BaCO_3$ which decarbonates into barium oxide and oxygen vacancy when annealed. This is consistent with the Ba 3*d* spectra, which clearly show two Ba species. The, O 1*s* spectra can be fitted to four peaks, which can be assigned according to previous work [37-41] as summarized in Table 1. The three lower binding energy peaks between ca. 529 eV and 533 eV are attributed to oxygen in the BST, BaO/$BaCO_3$ phases and that chemisorbed on the surface as CO^{3-}, which we collectively denote here as (O_1). The highest binding energy peak between 533.83 eV to 534 is attributed to the presence of oxygen defects (O_2) [38,39]. It is evident from the integrated areas that the $O_2/(O_1+O_2)$ decreases with increasing annealing

temperature, indicating that defects formed during the sputtering process are increasingly eliminated with increasing annealing temperature. This is consistent with the increase of binding energy with increasing annealing temperature seen in the Ba 3*d*, Sr 3*d* and Ti 2*p* spectra.

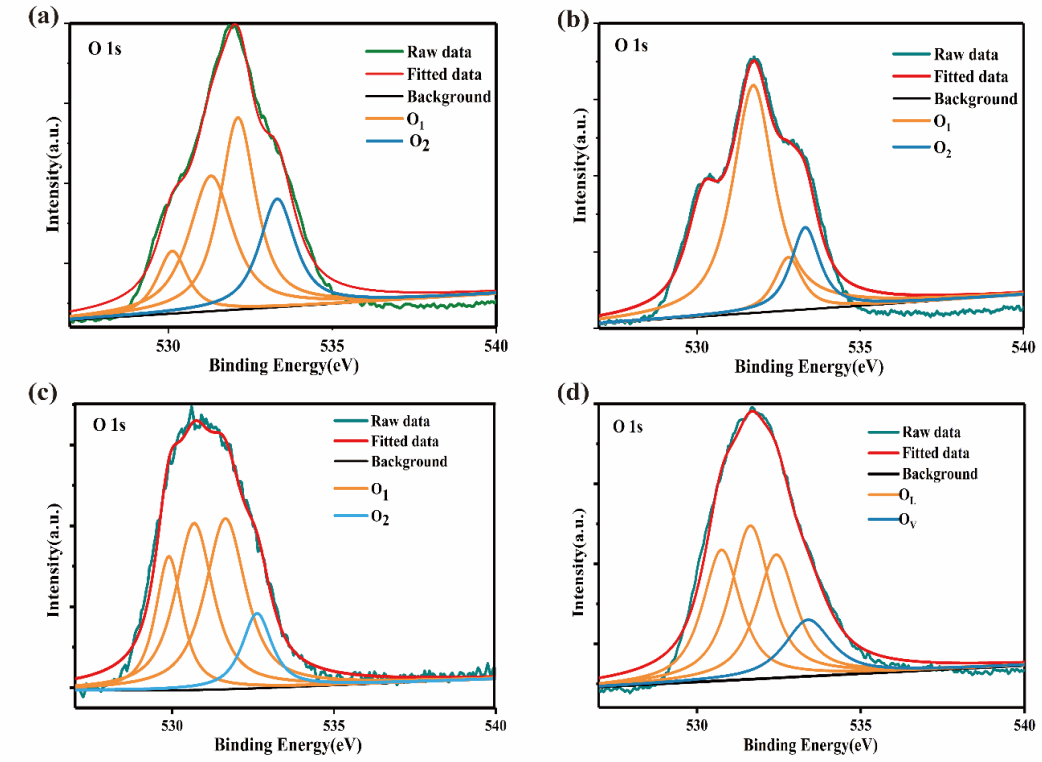

Fig. 4. O 1s X-ray photoelectron spectra for BST@C_f annealed at (a) 537 K, (b) 637 K, (c) 737 K and (d) 837 K.

Table 1: O1s X-ray photoelectron spectral assignments and defect oxygen percentages (%O_2) for un-annealed BST@C_f and BST@C_f annealed at 537 K, 637 K 737 K and 837 K.

Un-annealed BST@C_f	473K	573K	673K	773K

O_1 binding energies (eV)	531.00 532.23 533.00	530.13 531.31 532.13	530.19 531.73 532.80	529.90 530.68 531.64	530.73 531.61 532.47
O_2 binding energies (eV)	533.83	533.33	533.31	533.00	533.59
$O_2/(O_1+O_2)$	21.98%	20.84%	14.53%	11.66%	9.03%

3.2 Electrical properties

Electrical properties of BST@C_f were measured after 3000 times bent. As shown in Fig. 1, the un-annealed BST@C_f was connected to the top electrode while the annealed fibers were connected to the grounded bottom electrode. Current-voltage (I-V) curves for the four studied devices are shown in Fig. 5 on logarithmic scales with the linear scale plots inset. In each case, sweep limits were determined by initial experiments, gradually increasing the sweep width. All four devices show bipolar figure-of-eight (f8) type hysteresis loops, typical characteristics of memristors. Each of the logarithmic plots can be divided into three stages. Taking that for device H_1 as a representative example, when the voltage varies from 0 V to -1.5 V, the current increases gradually to 10^{-4} A, which defines the SET process. As the sweep reverses from -1.5 V to 0 V, the current decreases as the voltage approaches 0 V. defining the RESET process. When the voltage goes from -1.5 V to 1.5 V, the current retains high level except for the zero point, which is attributed to the equipment. Fig. 5(e)

illustrates the variation of resistance values during this cycle. During the SET process, the resistance switches from the high-resistance state (HRS) to the low-resistance state (LRS). As the voltage sweeps from -1.5 V to 1.5 V, the resistance remains at the LRS, confirming the device has the capability of maintaining the LRS in the power off state. During the RESET process, the resistance is switched back to the HRS. It is worth noting that unlike most memristors, which require extra large voltage as electroforming stimuli [3-6], there are no electroforming voltage required over the period of the switching process.

The observed electrical behavior can be explained by the motion of oxygen vacancies and interstitials (V_O and O_i). The un-annealed BST@C_f possess high concentrations of oxygen defects due to the sputtering process. As seen in the XPS results, the defect concentration decreases with increasing annealing temperature. Therefore, a concentration gradient in defects is generated between the two cross connected fibers and this gradient increases with increasing annealing temperature. Diffusion of V_O occurs as a result of the electric field [42, 43], with the vacancies possessing an effective positive charge attracted to the negative electrode, while O_i with an effective negative charge are attracted to the positive electrode. Conductive filaments gradually form between the two fibers during the SET process, which causes the device to attain the LRS of device. During the RESET process, a reverse voltage drives the defects in the reverse directions back breaking the conductive filament and leading to the HRS. The areas in the figure-of-eight loops of the I-V

plots are an indication of the strength of the filaments, with narrow loops indicating weaker filaments. In the case of devices H_1 to H_3 wide loops are seen, while the loop for device H_4 during the SET process is narrow and wide during the RESET process. This is likely related to the larger vacancy concentration gradient between the two fiber types in device H_4, with weak filaments produced in during the SET process. High defect concentrations increase the possibility and rate of defect migration, leading to stronger conductivity filaments. Hence, device H_4 with lowest defect concentration in the annealed fiber needed higher potential (a larger maximum potential was required) to build conductive filaments. In contrast, for device H_1 where defect concentration was high causes that the cut-off voltage required was small and the hysteresis loops were wide.

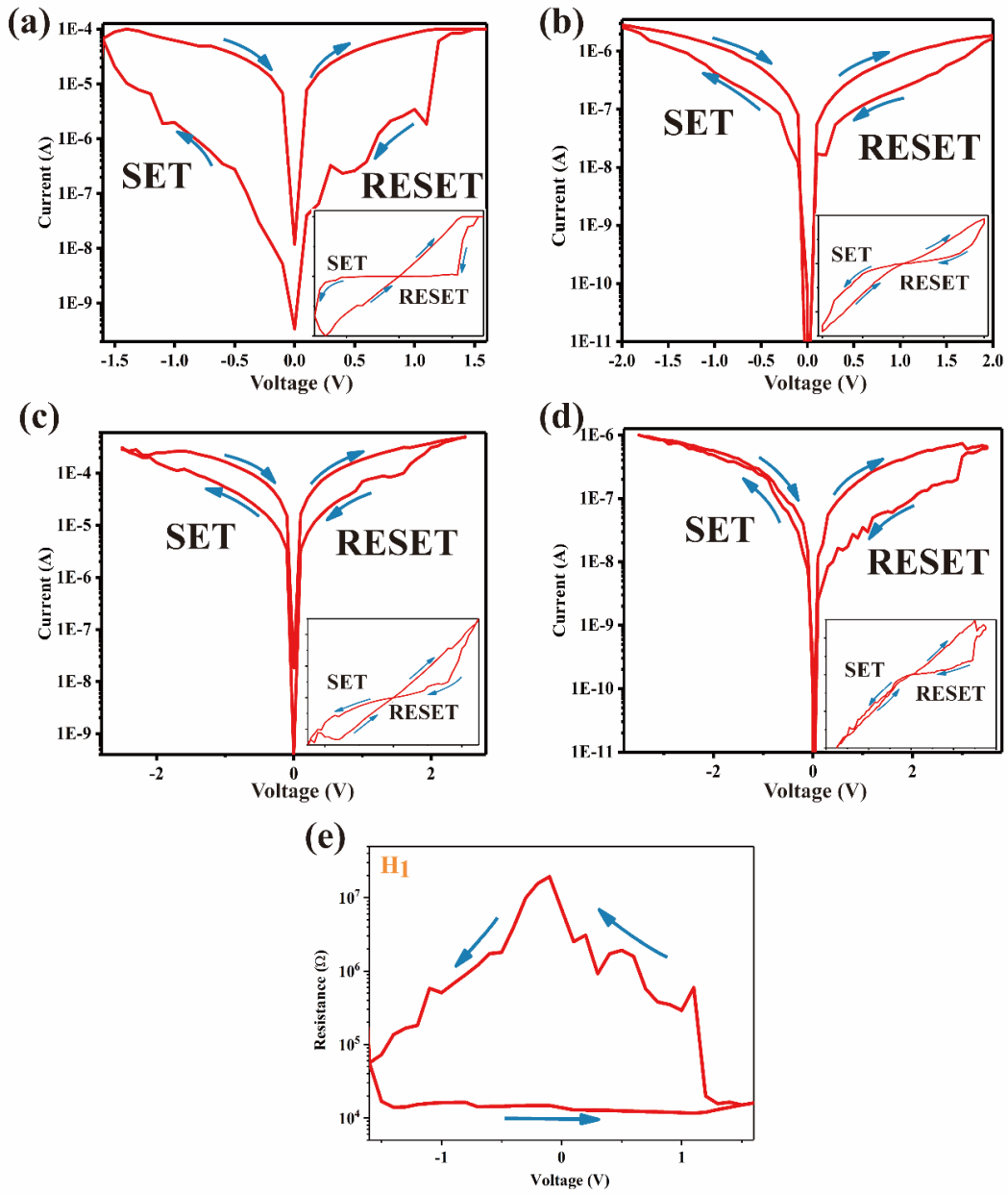

Fig. 5. Logarithmic scale I-V curves for devices (a) H_1, (b) H_2, (c) H_3 and (d) H_4, with linear scale plots inset; (e) resistance-voltage (R-V) curve for device H_1.

To test the cycling characteristics of devices H_1-H_4, bias potentials of -5 V, +5 V and were used as SET, RESET and voltages, respectively. The switching current of H_1 to H_4 of HRS and LRS during cycling test are show in Fig. 7(a) to Fig. 7(d). The number of times each group of devices can be cycled is counted in the Fig. 6(a). The results demonstrate that the cyclability of H_1 to H_4 devices decreases in the order of

increasing annealing temperature. The HRS and LRS values for device H_1 are plotted as a function of cycle number in Fig. 6(b). This device shows good cyclability during 1000 cycles. During cycling, oxygen defects are gradually eliminated through vacancy-interstitial recombination [44]. This reduction in defect concentration on continued cycling is likely to be the main cause of failure in the BST@C_f memristors. As a result, the defect concentrations of devices with fibers with low initial concentrations will deplete faster compared to those with higher defect concentrations, causing them to lose effectiveness after fewer cycles. In contrast, it is more difficult to exhaust the supply of defects in devices with high initial defect concentrations, resulting in extended cycling durability.

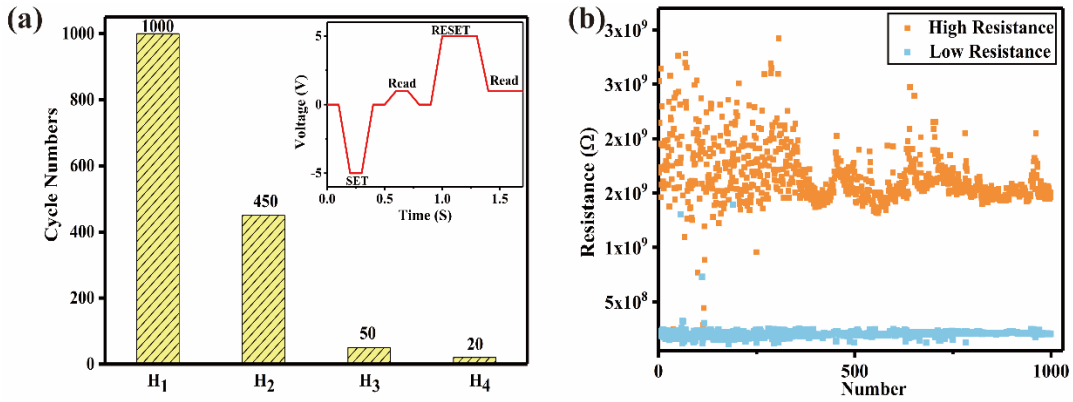

Fig. 6. (a) Maximum cycle numbers achieved for devices H_1 to H_4, with pulse sequence inset; (b) resistance values for the HRS and LRS of device H_1 over 1000 cycles.

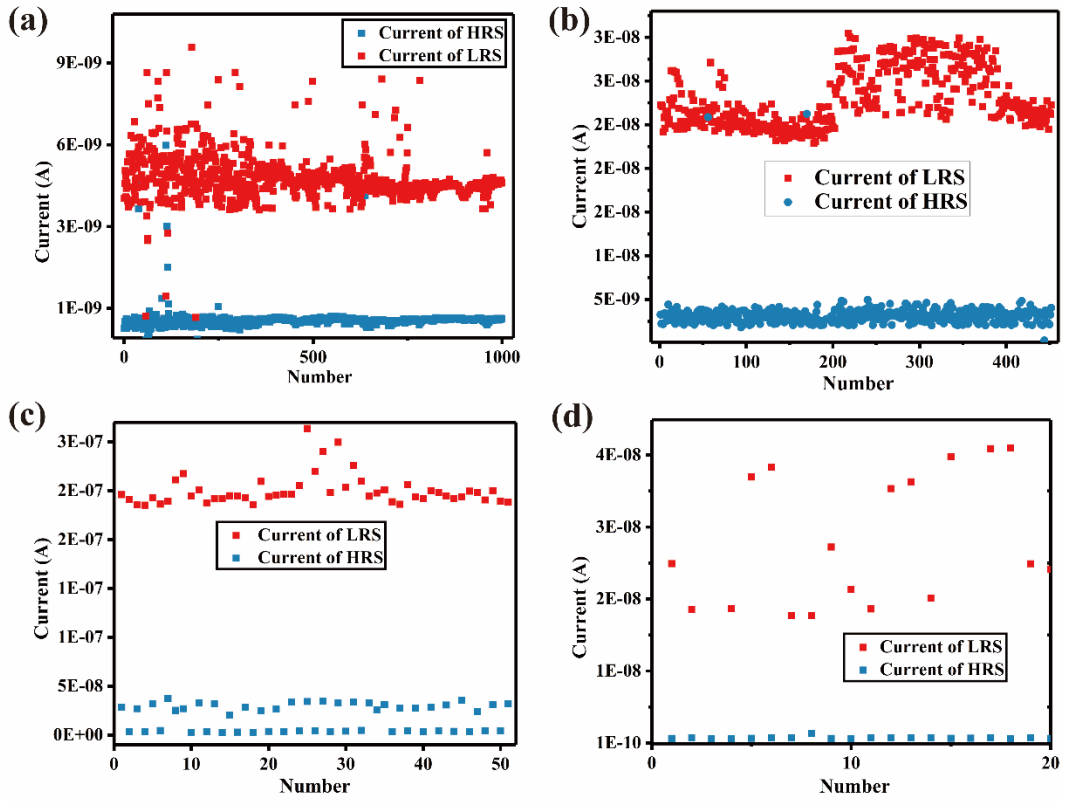

Fig. 7. The switching current of (a) H1, (b) H2, (c) H3, (d) H4 of HRS and LRS during cycling test.

One of the most important characteristics of memristors is memory retention after the SET process even in the power off state. In this study, memory retention was measured for device H_1 (Fig. 8). An initial potential of 1 V was to test the original state of the device (note that in this device, the un-annealed fibers were connected to the top electrode). A potential of +5 V was then applied as the SET voltage and power then immediately cut. After about 787 seconds a potential of 1 V was applied as a read voltage. As Fig. 8 demonstrates, the current of original state is ca. 10^{-9} A and changes to 10^{-6} A during the SET process, causing the device to switch from the HRS to the LRS. After the SET and cut off processes, the resistance increases slightly to 10^{-7} A, but is still in the LRS state. The memory retention test illustrates the potential of

BST@C_f memristors for application in electronic devices required to maintain data during periods of power failure.

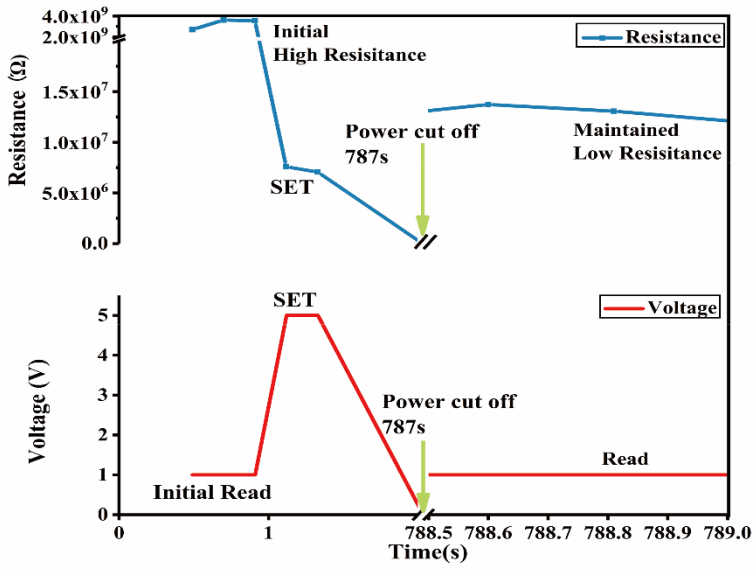

Fig. 8. Memory retention characteristics of device H_1 during power cut off for 786 s, showing voltage (lower) and resistance (upper) curves.

3.3 Interpretation theory of resistance transition process

There are several theoretical models proposed to explain the resistive switching process in memristors, such as Schottky emission, Fowler-Nordheim (F-N) tunneling, Poole-Frenkel emission and space-charge-limited conduction [45-47]. Among them, Schottky emission and F-N tunneling are commonly used to describe the resistance switching processes of perovskite-oxide memristors. The two theories indicate that current and voltage obey the relations:

$$\ln I \propto \sqrt{V} \tag{1}$$

and

$$(\ln \frac{I}{V} \propto \sqrt{V}) \tag{2}$$

during the SET process, respectively (where I and V are current and voltage, respectively). The experimental I-V data for device H_1 were fitted with MATLAB software based on equations (1) and (2) and the fitting results are shown in Fig. 9(a) and Fig. 9(b). The SET process can be divided into two parts: 0 V to -1.5 V and -1.5 V to -2.5 V. Fig. 9(c) and Fig. 9(d) show the transport model of carriers in these two continuous processes. During the 0 V to -1.5 V region, the plot of ln(I) vs. $\sqrt{V}$ is reasonably well fitted to a straight line with slope of 2.61, which means the process can be attributed to Schottky Emission. According previous researches [27,46], the BST@C_f is equivalent to two head-to-head Schottky diodes. The two diodes operate in opposite regime: the diode connected with the anodic is forward biased while the diode connected with the cathode electrode is reversely biased. In Schottky emission, under negative potential oxygen vacancies are driven to the positive electrode by the electric field and accumulate at the interface between BST and carbon fiber (C_f). This occurs over the potential range 0 to -1.5 V and leads to the depleted region W_1 decreasing gradually. During the increasing the voltage from -1.5 V to -2.5 V (Fig. 5d), the depletion region decreases to W_2 and allows electrons to tunnel from C_f to BST through the thin depletion region i.e. F-N tunneling. As can be seen in Fig. 9(b), over the range -1.5 V to -2.5 V, the plot of ln(I/V) vs. V^{-1} is linear with a slope of -2.44, indicating that F-N Tunneling is the dominant carrier transport process in this voltage range (Fig. 9(d)). (Electron affinity of BST (X_{BST}) and work function of carbon fiber (W_{cf}) can be referred to the previous work of Scott [49] and Hu [27], respectively.)

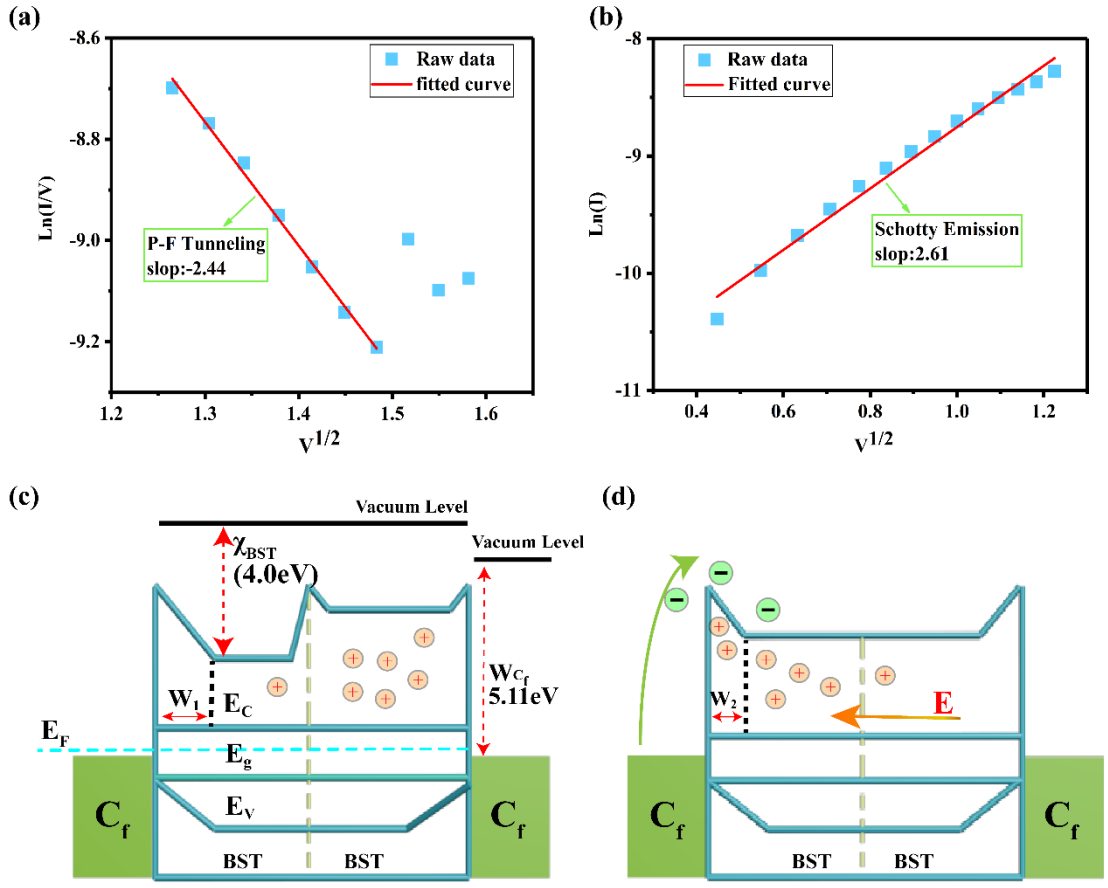

Fig. 9. Fits to (a) Eq. (1) (Schottky emission) and (b) Eq. (2) (F-N tunneling) for current voltage data for device H_1 over the respective voltage ranges 0 to -1.5V and -1.5 to -2.5 V. Schematics showing carrier transport processes during (c) Schottky emission and (d) F-N tunneling. E_C, E_g and E_V represent conduction band, forbidden band and valence band, respectively.

3.4 Synaptic simulation

Fig. 10(a) shows a schematic of a biological synapse. When continuous stimuli are applied to the synapse, the postsynaptic response of the later stimuli is higher than that of the initial one. This mechanism is called paired-pulse facilitation (PPF) [50,51], which is related to learning strengthened processes. When two stimuli are applied to a synapse, the second stimulus causes the presynaptic to release higher concentrations of ionic species (Na^+, Ca^{2+}, Mg^{2+}, etc.). As Fig. 10(b) illustrates, on continuous

sweeping between 0 V and +5 V voltage for 10 cycles, the current increases as the number of cycles increases. We applied cyclic pulses to H_1, the pulse amplitude, duration time and interval time are 1V, 0.001s and 0.001s. The performance of BST@C_f memristor is analogous to a biological synapse when applied to continuous voltage. The cyclic results are shown in Fig. 10(d). The current of the device increases with successive voltage and eventually reaches a limit., the current continuously increases obeying the PPF law:

$$\mathrm{PPF} = \frac{(G_2 - G_1)}{G_1} \times 100\% \quad (3)$$

where G_1 and G_2 are the conductance of the earlier and later pulses. Analysis of the data for device H_1 reveals the maximum PPF can reach 5.8%, and minimum PPF is about 0.36%. The PPF result demonstrating that the BST@C_f memristor has the potential to mimic synapses.

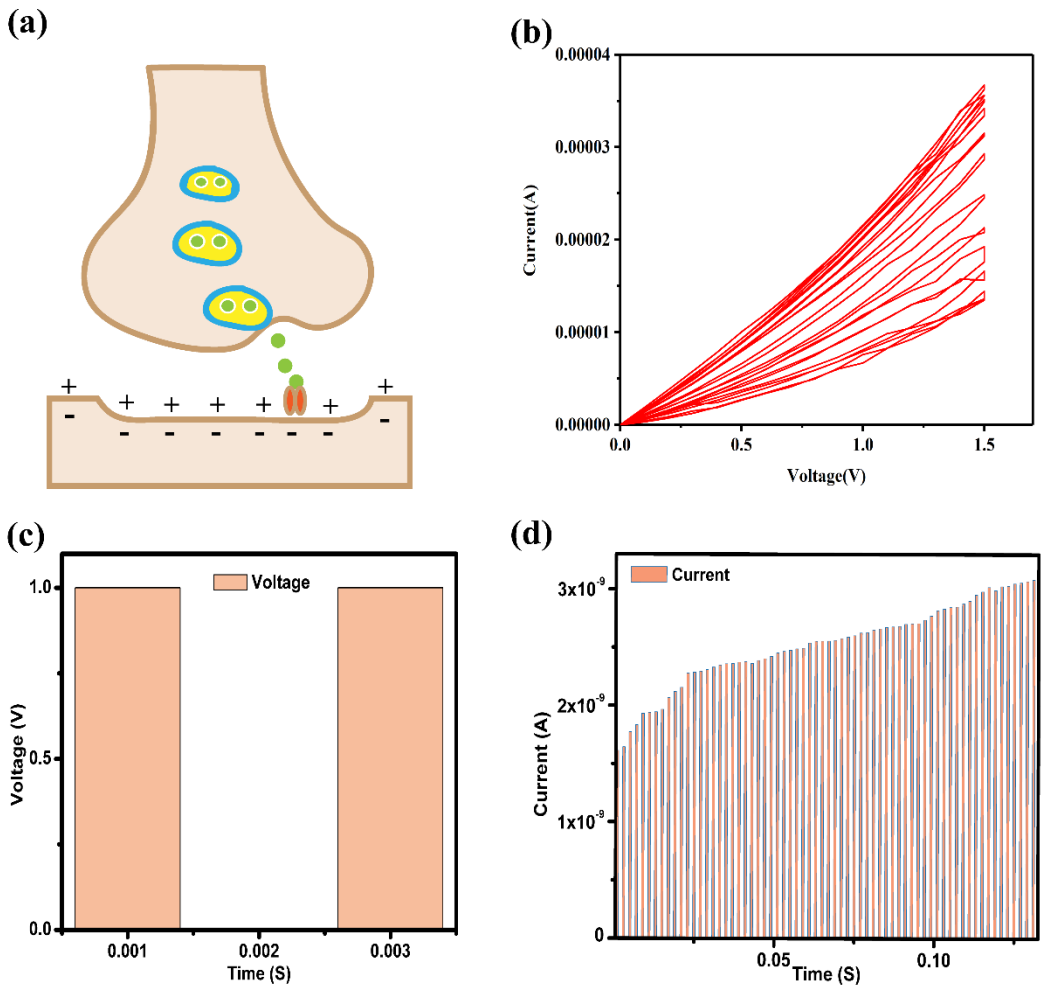

Fig. 10. (a) Schematic diagram of a biological synapse; (b) Change of current on 10 consecutive sweeps from 0 to +1.5 V. (c) The pulse of PPF test. (d)The gradually increasing current of H1 under continuous pulses.

4. Conclusions

In this study, BST was successfully used as a memory layer to construct a flexible memristor based on carbon fibers. Annealing the magnetron sputtered carbon fibers at different temperatures led to BST coatings containing different defect concentrations. Devices were constructed using cross connected BST coated fibers of different defect concentration. After being bent 3000 times, the electrical resulting of BST@C_f

memristors exhibited typical bipolar f8 hysteresis loops. The hysteresis loops demonstrate the switching process of resistance between high resistance state (HRS) and low resistance state (LRS), with a maximum HRS/LRS ratio of 10^6.

The switching process in BST@C_f memristors can be divided into two parts, which are well explained by Schottky emission and F-N tunneling. BST@C_f memristors with fibers containing high defect concentrations gradient showed excellent cyclability and memory retention behavior during power cut off. Additionally, the BST@C_f memristors obey the PPF law due to conductance increasing with increasing number of voltage cycles mimicking the strengthened learning process of biological synapses. Mounted on a flexible polymer BST@C_f based memristors have potential applications in wearable flexible electronic devices.

Acknowledgments

The work was supported by the Science and Technology Plan Project of Hunan Province Grant No. 2015TP1007; Initial Research Funding for Special Associate Professor by Central South University Grant No. 202045002; National Natural Science Foundation for Young Scientists of China No. 51802353; National Natural Science Foundation for Young Scientists of China No. 51602350.

References

[1] P.M. Solomon, Analog neuromorphic computing using programmable resistor arrays, Solid-State Electronics 155 (2019) 82–92, https://doi.org/10.1016/j.sse.2019.03.023.

[2] M.A. Zidan, A. Chen, G. Indiveri, W.D. Lu, Memristive computing devices and applications, J Electroceram (2017) 39:4–20, https://doi.org/10.1007/s10832-017-0103-0.

[3] W. Yi, K.K. Tsang, S.K. Lam, X. Bai, J.A. Crowell, E.A. Flores, Biological Plausibility and Stochasticity in Scalable V_O Active Memristor Neurons, Nat. Commun. (2018) 9:4661, https://doi.org/10.1038/s41467-018-07052-w.

[4] S. Kwon, T.W. Kim, S. Jang, J. Lee, N.D. Kim, Y. Ji, C. Lee, J.M.T our, G. Wang, Structurally Engineered NanoporousTa_2O_{5-x} Selector-Less Memristor for High Uniformity and Low Power Consumption, ACS Appl. Mater. Interfaces (2017) 34015-34023, https://doi.org/10.1021./acsami.7b06918.

[5] J. Wang, D. Ren, Z. Zhang, H. Xiang, J. Zhao, et al, A Radiation-hardening Ta/Ta2O_{5-x}/Al_2O_3/ $InGaZnO_4$ Memristor for Harsh Electronics, Appl. Phys. Lett. 113,122907 (2018); https://doi.org/10.1063/1.5045649.

[6] P. Cheng, K. Sun, Y.H. Hu, Memristive Behavior and Ideal Memristor of 1T Phase MoS_2 Nanosheets, Nano Lett. 16 (2016) 572−576, https: //doi.org/10.1021/acs.nanolett.5b04260.

[7] G.U. Siddiqui, M.M. Rehman, K.H. Choi, Enhanced resistive switching in all-printed, hybrid and flexible memory device based on perovskite $ZnSnO_3$ via PVOH polymer, Polymer 100 (2016) 102-110, http://dx.doi.org/10.1016/j.polymer.2016.07.081.

[8] B. Zhang, F. Fan, W. Xue, G. Liu, Y. Fu, et.al, Redox gated polymer memristive processing memorvitive unit, Nat. Commun. (2019) 10:736, https://doi.org/10.1038/s41467-019-08642-y.

[9] G. Zhou, X. Yang, L. Xiao, B. Sun A. Zhou, Investigation of a submerging redox behavior in Fe_2O_3 solid electrolyte for resistive switching memory, Appl. Phys. Lett. 114 (2019) 163506.1-163506.5, https://doi.org/10.1063/1.5089147.

[10] G. Zhou, Z. Ren, L.Wang, B. Sun, S. Duan, Q. Song, Artificial and wearable albumen protein memristor arrays with integrated memory logic gate functionality, Mater. Horiz. 6 (2019) 1877-1882, https://doi: 10.1039/c9mh00468h.

[11] G. Zhou, S. Duan, P. Li, B. Sun, B. Wu, et al, Coexistence of Negative Differential Resistance and Resistive Switching Memory at Room Temperature in TiOx Modulated by Moisture, Adv. Electron. Mater. 2018, https:// DOI: 10.1002/aelm.201700567.

[12] G. Zhou, Z. Ren, B. Sun, J. Wu, Z. Zou, S. Zheng, et al, Capacitive effect: an original of the resistive switching memory, Nano Energy 68 (2020) 104386, https://doi.org/10.1016/j.nanoen.2019.104386.

[13] G. Zhou, J. Wu, L. Wang, B. Sun, Z. Ren, et al, Evolution map of the memristor: from pure capacitive state to resistive switching state, Nanoscale 11 (2019) 17222-17229, https://doi: 10.1039/x0xx00000x.

[14] G. Zhou, Z. Ren, L. Wang, J. Wu, B. Sun, et al, Resistive switching memory integrated with amorphous carbon-based nanogenerators for self-powered device, Nano Energy 63 (2019) 103793, https://doi.org/10.1016/j.nanoen.2019.05.079.

[15] A.V. Babu, S. Lashkare, U. Ganguly, B. Rajendran, Stochastic learning in deep neural networks based on nanoscale PCMO device characteristics, Neurocomputing, 321 (2018) 227–236, https://doi.org/10.1016/j.neucom.2018.09.019.

[16] S. Choi, S. Jang, J. Moon, J.C. Kim, H.Y. Jeong, et al, A self-rectifying T_aO_y/nanoporous TaOx memristor synaptic array for learning and energy-efficient neuromorphic systems, NPG Asia Materials (2018) 10: 1097-1106, https://doi.org/10.1038/s41427-018-0101-y.

[17] T. Wang, Z. He, H. Liu, L. Chen, H. Zhu, et al, Flexible Electronic Synapses for Face Recognition Application with Multimodulated Conductance States, ACS Appl. Mater. Interfaces 10 (2018) 37345−37352, DOI: 10.1021/acsami.8b16841.

[18] Zhou, Y. Yao, Z. Lu, X. Yang, J. Han, et al, Hydrogen-peroxide-modified egg albumen for transparent and flexible resistive switching memory, Nanotechnology 28 (2017) 425202, https://doi.org/10.1088/1361-6528/aa8397.

[19] Q.A. Vu, H. Kim, V.L. Nguyen, U.Y. Won, S. Adhikari, et al, A High-On/Off-Ratio Floating-Gate Memristor Array on a Flexible Substrate via CVD-Grown Large-Area 2D Layer Stacking, Adv. Mater. 29 (2017) 1703363, https://doi.org/10.1002/adma.201703363.

[20] Y. Burgt, E. Lubberman, E.J. Fuller, S.T. Keene, G.C. Faria, A non-volatile organic electrochemical device as a low-voltage artificial synapse for neuromorphic computing, NATURE MATERIALS 16 APRIL 2017, https://doi.org/10.1038/NMAT4856.

[21] W. Xu, Y. Lee, S.Y. Min, C. Park, T.W. Lee, Simple, Inexpensive, and Rapid Approach to Fabricate Cross-Shaped Memristors Using an Inorganic-Nanowire Digital-Alignment Technique and a One-Step Reduction Process, Adv. Mater. 2016.28.527-532, https://doi.org/10.1002/adma.201503153.

[22] L. Koch, A. Polek, S. Rudd, D. Evans, Macroscopic Electrical Wires from Vapor Deposited Poly(3,4-ethylenedioxythiophene), ACS Appl. Mater. Interfaces 2017, 9, 65-70, https://doi.org/ ACS Appl. Mater. Interfaces 2017, 9, 65-70.

[23] H. Bae, B.C. Jang, H. Park, S. Jung, H.M. Lee, et al, Functional Circuitry on Commercial Fabric via Textile-Compatible Nanoscale Film Coating Process for Fibertronics, Nano Lett. 2017, 17, 6443−6452, https://doi.org/ DOI: 10.1021/acs.nanolett.7b03435.

[24] S.N. Truong, K.V. Pham, W. Yang, A. Jo, M.J. Lee, et al. Time-Shared Twin Memristor Crossbar Reducing the Number of Arrays by Half for Pattern Recognition, Nanoscale Research Letters (2017) 12:205, https://doi.org/ DOI 10.1186/s11671-017-1973-4.

[25] N. Liu, Z. Pan, X. Ding, J. Yang, G. Xu, In-situ growth of vertically aligned nickel cobalt sulfide nanowires on carbon nanotube fibers for high capacitance all-solid-state asymmetric fiber-supercapacitors, Journal of Energy Chemistry 41 (2020) 209–215, Journal of Energy Chemistry 41 (2020) 209-215.

[26] Y. Cohen, S.K. Reddy, Y. Ben-Shimon, A. Yaakobovitz, Height and morphology dependent heat dissipation of vertically aligned carbon nanotube, Nanotechnology 30 (2019) 505705 (7pp), https://doi.org/10.1088/1361-6528/ab424e.

[27] S. Hu, J. Yue, C. Jiang, X. Tang, X. Huang, et al, Resistive switching behavior and mechanism in flexible TiO_2@C_f memristor crossbars, Ceramics International 45 (2019) 10182-10186, https://doi.org/10.1016/j.ceramint.2019.02.068.

[28] J. Cui, G. Dong, Z. Yang, J. Du, Low dielectric loss and enhanced tunable properties of Mn-doped BST/MgO composites, Journal of Alloys and Compounds 490 (2010) 353-357, https://doi.org/10.1016/j.jallcom.2009.09.185.

[29] K. Nadaud, C. Borderon, R. Renoud, A. Ghalem, A. Crunteanu, et al, Effect of the incident power on permittivity, losses and tunability of $BaSrTiO_3$ thin films in the microwave frequency range, APPL. Phys. Lett. 110 (2017) 212902, https://doi.org/10.1063/1.4984089.

[30] K. Nadaud, C. Borderon, R. Renoud, A. Ghalem, A. Crunteanu, et. al, Domain wall motions in BST ferroelectric thin films in the microwave frequency range, Appl. Phys. Lett. 109(2016) 262902 https://doi.org/10.1063/1.4973451.

[31] K. Nadaud, C. Borderon, R. Renoud, A. Ghalem, A. Crunteanu, et. al, Diffuse phase transition of BST thin films in the microwave domain, Appl. Phys. Lett. 112 (2018) 262901, https://doi.org/10.1063/1.5030485.

[32] X. Fu, X. Zeng, T, Cui, C. Lan, Y. Guo et al, Mode jumping of split-ring resonator metamaterials controlled by high-permittivity BST and incident electric fields, Scientific REPORTS (2016) 6:31274, https://doi.org/10.1038/srep31274.

[33] C.S. Hwang, S.O. Park, H. Cho, C.S. Kang, H. Kang et al, Deposition of extremely thin (Ba,Sr)TiO_3 thin films for ultra-large-scale integrated dynamic random access memory application, Appl. Phys. Lett. 67 (1995) 2819, https://doi.org/10.1063/1.114795.

[34] Y. Li, G. Dou, TOWARDS THE IMPLEMENTATION OF MEMRISTOR: A STUDY OF THE ELECTRIC PROPERTIES OF $Ba_{0.77}Sr_{0.23}TiO_3$ MATERIAL, International Journal of Bifurcation and Chaos, Vol. 23, No. 12 (2013) 1350204, https://doi.org/10.1142/S0218127413502040.

[35] Y. Fujisaki, Y. Shimamoto, Y. Matsui, Analysis of Decomposed Layer Appearing on the Surface of Barium Strontium Titanate, Jpn. J. Appl. Phys. 8 (1999) L 52–L 54, https://doi.org/110.53.160.179.

[36] A. Rodrigues, S. Bauer, T. Baumbach, Effect of post-annealing on the chemical state and crystalline structure of PLD $Ba_{0.5}Sr_{0.5}TiO_3$ films analyzed by combined synchrotron X-ray diffraction and X-ray photoelectron spectroscopy, Ceramics International 44 (2018) 16017-16024, https://doi.org/10.1016/j.ceramint.2018.06.038.

[37] Y.H. Gao, H. Shen, J.H. Ma, J.Q. Xue, J.L. Sun, et al, Surface chemical composition and optical properties of nitrogen-doped thin films, J. Appl. Phys. 102 (2017) 064106, https://doi.org/10.1063/1.2783999.

[38] Z. Saroukhani, N. Tahmasebi, S.M. Mahdavi, A. Nemati, Effect of working pressure and annealing temperature on microstructure and surface chemical composition of barium strontium titanate films grown by pulsed laser deposition, Bull. Mater. Sci. 38 (2015) 1645–1650, https://doi.org/10.1007/s12034-015-0982-0.

[39] C. Norman, C. Leach, In situ high temperature X-ray photoelectron spectroscopy study of barium strontium iron cobalt oxide, Journal of Membrane Science 382 (2011) 158-165, https://doi.org/10.1016/j.memsci.2011.08.006.

[40] S. Acharya, J. Torgersen, Y. Kim, J. Park, P. Schindler, Self-limiting atomic layer deposition of barium oxide and barium titanate thin films using a novelpyrrole based precursor, J. Mater. Chem. C, 4 (2016) 1945, https://doi.org/10.1039/c5tc03561a.

[41] P.C. Nagajyothi, M. Pandurangan, T.V.M. Sreekanth, J. Shim, In vitro anticancer potential of $BaCO_3$ nanoparticles synthesized via green route, Journal of Photochemistry & Photobiology, B: Biology 156 (2016) 29–34, http://dx.doi.org/10.1016/j.jphotobiol.2016.01.008.

[42] R. Schmittt, M. Kubicek, E. Sediva, M. Trassin, M.C. Weber, et al, Accelerated Ionic Motion in Amorphous Memristor Oxides for Nonvolatile Memories and Neuromorphic Computing, Adv. Funct. Mater. 29 (2019) 1804782, https://doi.org/10.1002/adfm.201804782.

[43] F. Mei, H. Shen, L. Li, G. Zang, Y. Shao, Influence of Frenkel defects on endurance behavior in SnO_2:Cu memristors, J. Appl. Phys. 125 (2019) 074502, https://doi.org/10.1063/1.5084317.

[44] W. Zhang, Y. Mao, W. Duan, Synaptic and Digital Switching in Diffusion Effect-Assisted Oxides for All-Inorganic Flexible Memristor, Phys. Status Solidi RRL 13 (2018) 1900016, https://doi.org/10.1002/pssr.201900016.

[45] T. You, N. Du, S. Slesazeck, T. Mikolajick, G. Li, et al, Bipolar Electric-Field Enhanced Trapping and Detrapping of Mobile Donors in $BiFeO_3$ Memristors, ACS Appl. Mater. Interfaces 6 (2014) 19758−19765, https://doi.org/10.1021/am504871g.

[46] E.W. Lim, R. Ismail, Conduction Mechanism of Valence Change Resistive Switching Memory: A Survey, Electronics 4 (2015) 586-613, https://doi.org/10.3390/electronics4030586.

[47] Y. Li, Y.P. Zhong, J.J. Zhang, X.H. Xu, Q. Wang et al, Intrinsic memristance mechanism of crystalline stoichiometric $Ge_2Sb_2Te_5$, Appl. Phys. Lett. 103 (2013) 043501, https://doi.org/10.1063/1.4816283.

[48] Y. Yu, C. Wang, C. Jiang, I. Abrahams, Z. Du, et al. Resistive switching behavior in memristors with TiO_2 nanorod arrays of different dimensionsm, Applied Surface Science 485 (2019) 222-229, https://doi.org/10.1016/j.apsusc.2019.04.119

[49] J.F. Scott, K. Watanabe, A.J. Hartmann, R.N. Lamb, Device Models for PAT/Pt, BST/Pt, SBT/Pt, and SBT/Bi Ferroelectric Memories, Ferroelectrics, 225:1 83-90, http://dx.doi.org/10.1080/00150199908009114.

[50] Q. Xue, Y. Wang, X. Wei, Synaptic plasticity of room-temperature fabricated amorphous MoO_x film based memristor, Applied Surface Science 479 (2019) 469-474, https://doi.org/10.1016/j.apsusc.2019.02.092.

[51] X. Yan, Q. Zhao, A.P. Chen, J. Zhao, Z. Zhou, et al, Vacancy-Induced Synaptic Behavior in 2D WS_2 Nanosheet- Based Memristor for Low-Power Neuromorphic Computing, Small 15 (2019) 1901423, https://doi.org/10.1002/smll.201901423.